Nanoscale Advances

ROYAL SOCIETY OF CHEMISTRY

PAPER

View Article Online
View Journal | View Issue

Cite this: *Nanoscale Adv.*, 2025, **7**, 7538

Anomalous Raman signals in multilayer hexagonal boron nitride grown by chemical vapour deposition on metal foil catalysts

Takara Okonai,[a] Pablo Solís-Fernández,[b] Satoru Fukamachi,[b] Haiming Sun,[c] Yeri Lee,[d] Yung-Chang Lin,[e] Toshiaki Kato,[f] Sunmin Ryu,[d] Kazu Suenaga[c] and Hiroki Ago *[abg]

Received 26th March 2025
Accepted 13th August 2025

DOI: 10.1039/d5na00283d

rsc.li/nanoscale-advances

Hexagonal boron nitride (hBN), a two-dimensional (2D) wide bandgap material, serves as an ideal insulating substrate and a protection layer for other 2D materials, such as graphene and transition metal dichalcogenides (TMDs). Here, we report for the first time the emergence of an anomalous Raman peak in single-crystal, multilayer pyramidal hBN grains grown on Fe–Ni alloy foil by chemical vapour deposition (CVD). This peak is located near the characteristic E_{2g} band (1367 cm^{-1}) and shifts to higher wavenumbers with the increasing number of hBN layers, peaking at ~1415 cm^{-1} at the centre of hBN grains. The appearance of this Raman peak is attributed to a blue shift of the E_{2g} phonon caused by compressive strain induced during the cooling step in the CVD process. Triangular hBN grains are epitaxially grown on the alloy catalyst and hence are strongly affected by the volume change of the Fe–Ni alloy catalyst and by lateral compression induced by the steps of the Fe–Ni surface. The maximum strain calculated from the peak shift is −1.23%, which is much higher than the values previously reported for strained hBN, indicating a strong impact of the metal catalyst on the growing hBN structure. These results demonstrate the feasibility of strain engineering in hBN *via* CVD growth.

Introduction

Hexagonal boron nitride (hBN) has an atomically flat surface with a wide band gap of 5.9 eV,[1] as well as high thermal and chemical stability[2,3] and mechanical strength.[4] These properties make hBN an ideal substrate and protection layer for other two-dimensional (2D) materials, such as graphene and transition metal dichalcogenides (TMDs). Especially, multilayer hBN enables observation of the intrinsic physical properties of these 2D materials and boosts their carrier transport and light emission,[5–8] leading to the development of 2D electronics and photonics. In addition, hBN itself is promising for various applications, such as ultraviolet light emitters,[9] single photon emitters,[10] gas barriers,[3] ferroelectric devices[11] and van der Waals tunnelling barriers.[12]

There are several methods to synthesize hBN layers. The most common method is mechanical exfoliation, which produces flakes with high crystallinity, but with limited size and no control over their thickness. For the development of practical applications based on 2D materials, chemical vapour deposition (CVD) growth has attracted great interest, as it allows the growth of large-area hBN sheets.[13–16] Depending on the growth conditions and the employed catalyst, CVD-grown hBN shows varying crystallinity, grain sizes and defect densities. Therefore, assessing the quality of CVD-grown hBN is important for fundamental research as well as the development of applications.

Among the available methods to analyse hBN, especially in terms of quality and crystallinity, one of the most effective methods is Raman spectroscopy. The E_{2g} Raman band at ~1370 cm^{-1}, originating from the in-plane vibrations of B and N atoms moving in opposite directions,[17] gives important information on hBN. The intensity of the E_{2g} band increases linearly with the number of hBN layers, and the full width at half maximum (FWHM) reflects the crystallinity. The FWHM of hBN flakes exfoliated from single crystals is 8–9 cm^{-1},[18] while hBN with low crystallinity shows much larger FWHM values of >30 cm^{-1}.[19,20] In addition, as the E_{2g} band is influenced by interlayer coupling, its position also depends on the hBN

[a]*Interdisciplinary Graduate School of Engineering Sciences, Kyushu University, Fukuoka 816-8580, Japan. E-mail: ago.hiroki.974@m.kyushu-u.ac.jp*
[b]*Faculty of Engineering Sciences, Kyushu University, Fukuoka 816-8580, Japan*
[c]*The Institute of Scientific and Industrial Research (SANKEN), The University of Osaka, Osaka 567-0047, Japan*
[d]*Department of Chemistry, Pohang University of Science and Technology (POSTECH), Pohang 37673, Korea*
[e]*Nanomaterials Research Institute, National Institute of Advanced Industrial Science and Technology (AIST), Tsukuba 305-8565, Japan*
[f]*Graduate School of Engineering, Tohoku University, Sendai 980-8579, Japan*
[g]*Center for Semiconductor and Device Ecosystem (CSeDE), Kyushu University, Fukuoka 816-8580, Japan*

thickness; the E_{2g} band downshifts from 1370 cm^{-1} to 1366 cm^{-1} as the thickness increases from monolayer to few layer.[21,22] The E_{2g} position is also highly sensitive to applied strain, and it has been reported that tensile strain in hBN downshifts the E_{2g} band.[23,24]

Here, we demonstrate the emergence of an anomalous Raman peak in multilayer hBN grains grown by the catalytic CVD method. This Raman peak is prominent in triangular pyramidal grains and is located near the original E_{2g} band, shifting to higher wavenumbers with increasing hBN thickness. Assuming that the origin of this Raman peak is an upshift of the E_{2g} phonon caused by compressive strain, we examined this hypothesis by comparing the estimated strain from the peak shift of the unstrained E_{2g} band with the strain that could arise during the cooling step of CVD due to the large mismatch in thermal expansion coefficients between the metal catalyst and hBN. We found that the strain values estimated by these two approaches show good agreement, with the maximum compressive strain being as high as −1.23%, which exceeds previously reported values.

Experimental section

Synthesis and transfer of multilayer hBN

Multilayer hBN was synthesized by low-pressure CVD using borazine ($B_3N_3H_6$) as a feedstock. Fe–Ni alloy foil (Super Invar, 20 μm thickness, Nilaco), consisting of mainly Fe (∼64%) and Ni (∼32%), was used as a growth catalyst.[16] The pressure was maintained at ∼30 Pa during the CVD process. After annealing the Fe–Ni alloy foil at 1000 °C for 40 min in a H_2 flow, a controlled amount of borazine vapour was introduced by Ar carrier gas for hBN growth at 1200 °C for 30 min. The furnace was then cooled down to 700 °C at a cooling rate of 5 °C min^{-1}, followed by rapid cooling to room temperature.

The hBN transfer from Fe–Ni foil to SiO_2/Si was performed using an adhesive tape whose adhesion force can be tuned with ultraviolet (UV) light.[25] After attaching the UV tape to as-grown hBN, it was illuminated with UV light, and the tape/hBN was delaminated by electrochemical bubbling. After washing the tape/hBN stack with deionized water, the stack was attached to a SiO_2/Si substrate with an oxide layer thickness of 300 nm, and the UV tape was slowly peeled off, leaving the multilayer hBN on SiO_2/Si. For comparison, we also transferred hBN by protecting it with a thin film of polymethyl methacrylate (PMMA) instead of UV tape. The PMMA/hBN stack was detached from the Fe–Ni foil by either electrochemical bubbling or metal etching with a $FeCl_3$–HCl mixed solution. Finally, the PMMA film was removed with acetone.

Characterization

Optical microscope and atomic force microscope (AFM) images were obtained using a Keyence VHX-7000 and Bruker nanoscope V, respectively. Scanning electron microscopy (SEM) measurements were performed with a HITACHI S-4800 microscope. Cross-sectional images were acquired with a transmission electron microscope (TEM, Hitachi H-9500) and a scanning transmission electron microscope (STEM, JEOL ARM200F) equipped with a CEOS corrector operating at 200 kV. Electron energy loss spectroscopy (EELS) mapping was performed using a K3 camera installed in a Gatan Continuum GIF system. Raman spectra were measured with a Nanofinder 30 (Tokyo Instruments) using a 532 nm excitation laser, a 100× objective lens (0.90 NA) and a 1800 line/mm grating, with a spectral resolution of ∼0.71 cm^{-1}. The laser power was set to 10 mW with an exposure time of 4 s per point. The laser spot size was around 0.6 μm, and the measurement step size was set to 1 μm for mapping scans. The Raman spectra were baseline-corrected using the pybaselines Python package,[26] and peak separation was performed by curve fitting with pseudo-Voigt functions using the least-squares method with the lmfit Python package.[27] Polarized second harmonic generation (SHG) imaging was performed with a home-built micro-SHG spectroscopy setup configured on a commercial microscope (Ti–U, Nikon). As the fundamental beam, plane-polarized pulses at a wavelength of 800 nm, with a pulse duration of 140 fs, and a repetition rate of 80 MHz were generated using a commercial Ti : sapphire laser.

Results and discussion

Fig. 1a shows a SEM image of as-grown hBN on Fe–Ni foil, in which a number of triangular grains with lateral sizes of around 10–20 μm are observed. These grains are well aligned, suggesting the epitaxial growth of hBN within a grain of the metal alloy. We transferred the as-grown hBN film to a SiO_2/Si substrate and characterized it by optical microscopy and AFM, as shown in Fig. 1b and c for one of the hBN grains. These images indicate that the triangular grain has a pyramidal shape with its thickness increasing towards the centre of the hBN grain. We performed the SHG measurements of the pyramidal hBN grains, as shown in Fig. 1d. This SHG intensity mapping shows that there are no grain boundaries inside the grain, indicating its single-crystalline nature. In addition, the polarization analysis (Fig. S1) indicates that the hBN grain has zigzag edges. We observed an increase in the SHG intensity with the number of hBN layers, indicating that the grain does not have the most stable AA′ stacking.[28,29] This is because AA′-stacked hBN should exhibit low SHG intensity for an even number of layers due to centrosymmetric stacking. Therefore, it is highly likely that pyramidal hBN grains have a non-centrosymmetric stacking order, like AB stacking. Non-centrosymmetric stacking in multilayer hBN has attracted interest for memory applications due to its potential to exhibit ferroelectricity and antiferroelectricity through interlayer sliding.[11,30] Further studies on the stacking of triangular hBN grains are currently underway.

Several wrinkles are observed in the AFM image (Fig. 1c). These wrinkles run predominantly in three directions. Considering the grain orientation determined by the SHG (see Fig. S1e), the wrinkles are formed along the armchair direction. Wrinkles oriented in the armchair direction have been reported in the literature when hBN undergoes biaxial compression.[31,32] It is highly likely these wrinkles are formed upon cooling down

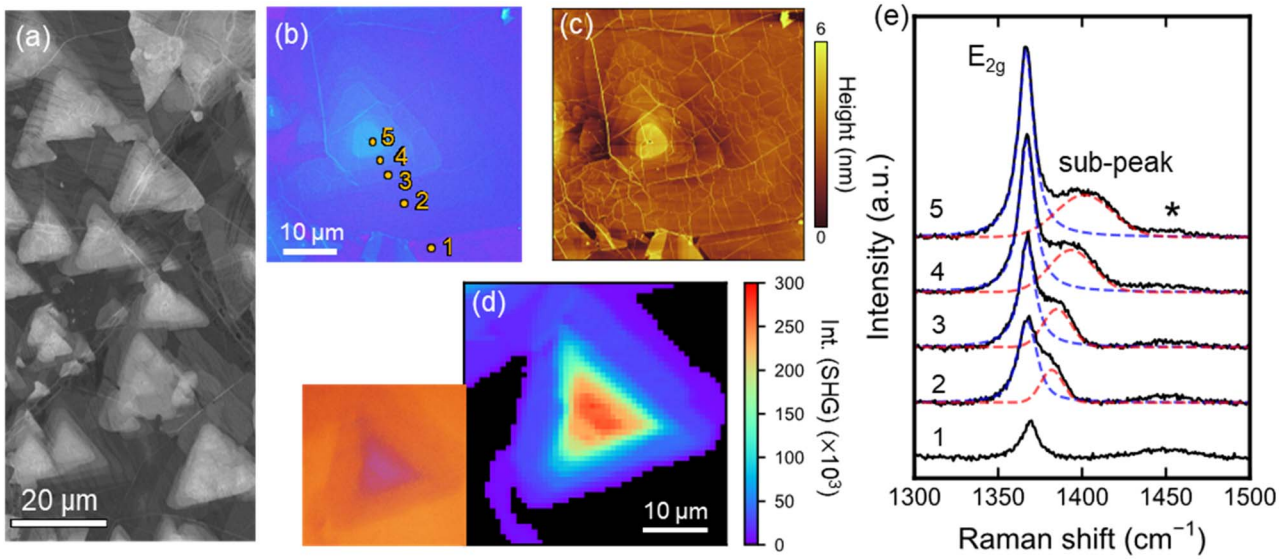

Fig. 1 (a) SEM image of as-grown multilayer hBN with a triangular pyramidal structure. Optical (b) and AFM (c) images of a hBN grain. (d) SHG intensity mapping of a hBN grain. Left panel displays the optical image. (e) Raman spectra measured at the marked positions shown in (b). Red and blue dashed lines are fitted curves, with the peak marked by an asterisk (*) being originated in the SiO_2 substrate.

during CVD due to the difference in the coefficients of thermal expansion (CTE) of hBN and the underlying alloy foil, as discussed later.

Fig. 1e shows Raman spectra of the triangular pyramidal grain collected at the positions marked in Fig. 1b. An intense E_{2g} band was observed at 1367 cm^{-1}, proving the formation of multilayer hBN. The intensity increased towards the centre of the grain, in agreement with optical and AFM observations. Interestingly, in addition to the original E_{2g} band, we observed a clear peak at higher wavenumbers (hereafter referred to as "sub-peak"). The Raman spectra in Fig. 1e were fitted using pseudo–Voigt functions with the three components observed in the spectra: the E_{2g} peak, the sub-peak and a broad peak originating from the SiO_2 substrate (1450.5 cm^{-1}). While the E_{2g} band position did not change for the different measured points, the sub-peak shifted to higher wavenumbers with increasing hBN thickness. While the E_{2g} band position shows only a minor thickness-dependent shift, converging to the bulk value (~1366 cm^{-1}) for thicker hBN,[21,22] the sub-peak shifts more markedly to higher wavenumbers with increasing thickness. We will later discuss this observation in light of our hypothesis that strain in hBN may underlie this behaviour. In addition, this sub-peak becomes broader with increasing hBN thickness. While the CVD growth of triangular multilayer hBN grains has been previously reported, there are no reports on the observation of such a peak.[33–36]

In contrast, the areas with uniform hBN thickness did not show the sub-peak, with only the E_{2g} band at 1367–1368 cm^{-1} (Fig. S2). The E_{2g} intensity in this area is weaker than that in Fig. 1b and c, from which we estimate the hBN thickness to be 3–6 hBN layers, based on our previous characterisation.[12] As the sub-peak was also absent outside the triangular pyramidal grain (point 1 in Fig. 1e), the presence of the sub-peak can be a characteristic feature of triangular grains.

For a more detailed analysis, Raman mapping was performed for the hBN grain shown in Fig. 1b and c. Fig. 2a displays the intensity of the E_{2g} band, which follows a mountain-like structure consistent with the optical and AFM images. On the other hand, the E_{2g} position was almost constant, falling within the range of 1365–1367 cm^{-1} (see Fig. S3a). The peak position and area (integral intensity) of the sub-peak are displayed in Fig. 2b and c, respectively. We can see that the area of the sub-peak increases when moving from the grain edge toward the centre. This increase of the area is mainly due to a broadening of the peak (Fig. S3c), which will be interpreted later. The sub-peak shifts to higher wavenumbers toward the centre of the trigonal grain, from ~1380 cm^{-1} at the edge to ~1410 cm^{-1} at the grain centre. This tendency of the Raman sub-peak was widely observed in other pyramidal hBN grains, as presented in Fig. S4–S6.

In Fig. 2d, the area of the sub-peak is plotted as a function of its position, while the colour of the dots represents the intensity of the E_{2g} band. There is a linear relationship between the sub-peak area and the intensity of the E_{2g} band. This suggests that the volume of the hBN layers which contribute to the sub-peak increases with the main E_{2g} component. However, as will be discussed later, we consider that the E_{2g} band and the sub-peak might originate from layers experiencing different levels of strain. Hence, their simultaneous increase suggests a consistent proportion of strained to unstrained layers across regions of varying thickness, supporting the strain gradient model proposed later.

It is noted that the appearance of the sub-peak does not depend on the transfer process and Raman measurement conditions. As shown in Fig. S7 and S8, we also observed the

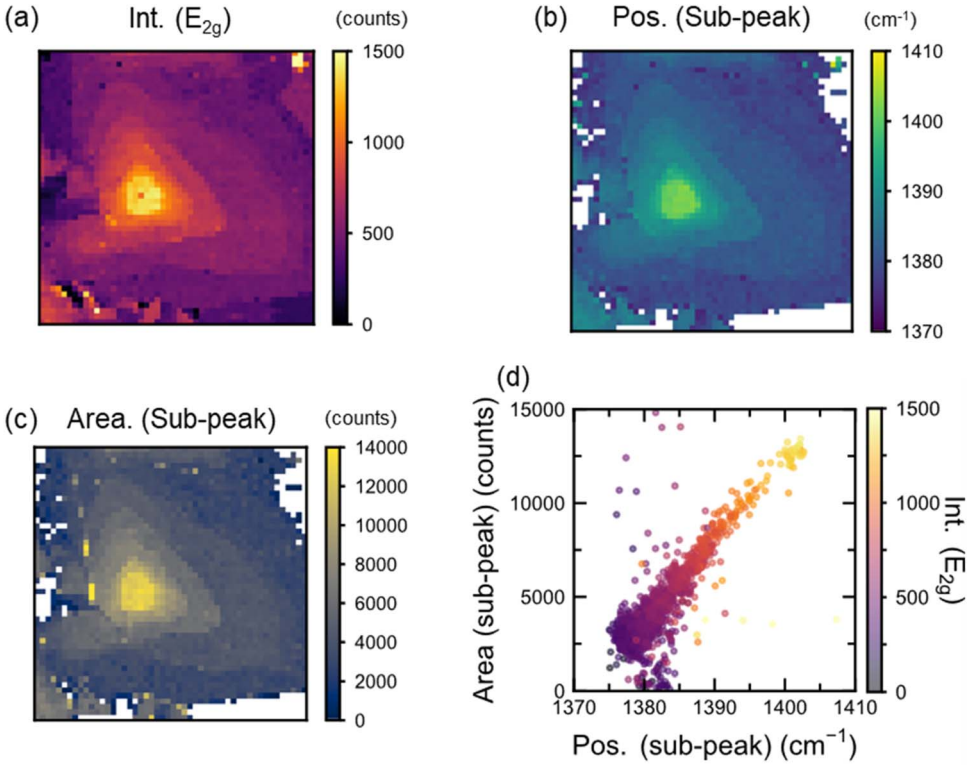

Fig. 2 Raman mappings of hBN E_{2g} intensity (a), sub-peak position (b) and area of the sub-peak (c). (d) Plot of the area of the sub-peak against its position. The colours of the plots indicate the intensity of the E_{2g} band. Here, the intensity and area mean the peak height and integrated area of each peak, respectively.

sub-peak when the hBN was transferred with the PMMA-support layer instead of the adhesive tape. Furthermore, we also observed the sub-peak when the sample was transferred onto a SiO_2/Si substrate with a 90 nm oxide layer (Fig. S9), and it appeared independently of the excitation wavelength, laser power, and irradiation time used (Fig. S10). Therefore, we believe that the origin of the sub-peak lies in the growth stage of hBN.

In the following, we discuss the possible reason for the emergence of the sub-peak in the Raman spectra of the triangular grains with pyramidal shape. There are several possible reasons, including the presence of other crystalline phases, defects, impurities (doping) and strain. Boron nitride crystals with cubic and wurtzite phases are known to exhibit Raman peaks at 1056 cm^{-1} (F_2(TO)), 1304 cm^{-1} (F_2(LO)) and at 950 cm^{-1} (A_1(TO)), 1015 cm^{-1} (A_1(LO)), 1050 cm^{-1} (E_1(TO)), and 1295 cm^{-1} (E_1(LO)),[17] respectively. Therefore, the observed sub-peak does not originate from these other crystalline phases of boron nitride. Cross-sectional TEM and STEM images and the elemental mapping for the grain in Fig. 3a are shown in Fig. 3b–d. We observed a well-ordered layered structure of hBN, with an average interlayer distance of 0.34 nm (Fig. 3c). No apparent defects and disorders were observed. As will be discussed below, the thickness of hBN seems to increase in steps of the Fe–Ni substrate (Fig. 3c). The EELS mapping (Fig. 3d) proves that the film consists of B and N atoms. Additionally, the EELS core-loss spectrum exhibited strong π* energy loss peaks at the K-shell edges of boron (~191 eV) and nitrogen (~401 eV) (Fig. 3e and S11), indicating that the pyramidal grain has sp^2 bonding.[37] Thus, combined with the observation of the narrow Raman E_{2g} band (FWHM being 12.3 ± 1.5 cm^{-1}) (Fig. S2b) and single crystallinity of the pyramidal hBN grain (Fig. 1d and S1), we can conclude that other crystalline phases and structural defects are not the origin of the sub-peak.

Impurities in hBN can locally alter lattice vibrations, through atomic substitution or changes in the bond length. Previous research reported that the intentional doping with Mg and GeO_2 during the growth process alters the Raman spectrum.[38–40] However, the EELS spectrum (Fig. 3e) indicates that the amount of possible impurities is lower than our detection limit. Moreover, the observed shift of the sub-peak relative to the E_{2g} band is much larger than that reported in previous literature for doping.[38–40] Therefore, it is also unlikely that the Raman sub-peak is related to impurities existing in the hBN lattice.

We hypothesize that the strain induced during the CVD process, especially when cooling down from the high growth temperature (1200 °C) to room temperature is the main origin of the Raman sub-peak. It is acknowledged that compressive strain tends to shift the E_{2g} band to higher wavenumbers.[41,42] The sub-peak appears at the higher wavenumber side of the E_{2g} band, suggesting an upshift of the E_{2g} phonon caused by compressive strain. As will be discussed later, we attribute the presence of both the E_{2g} and the sub-peak in the same spectra to a vertical gradient of in-plane strain across the hBN layers,

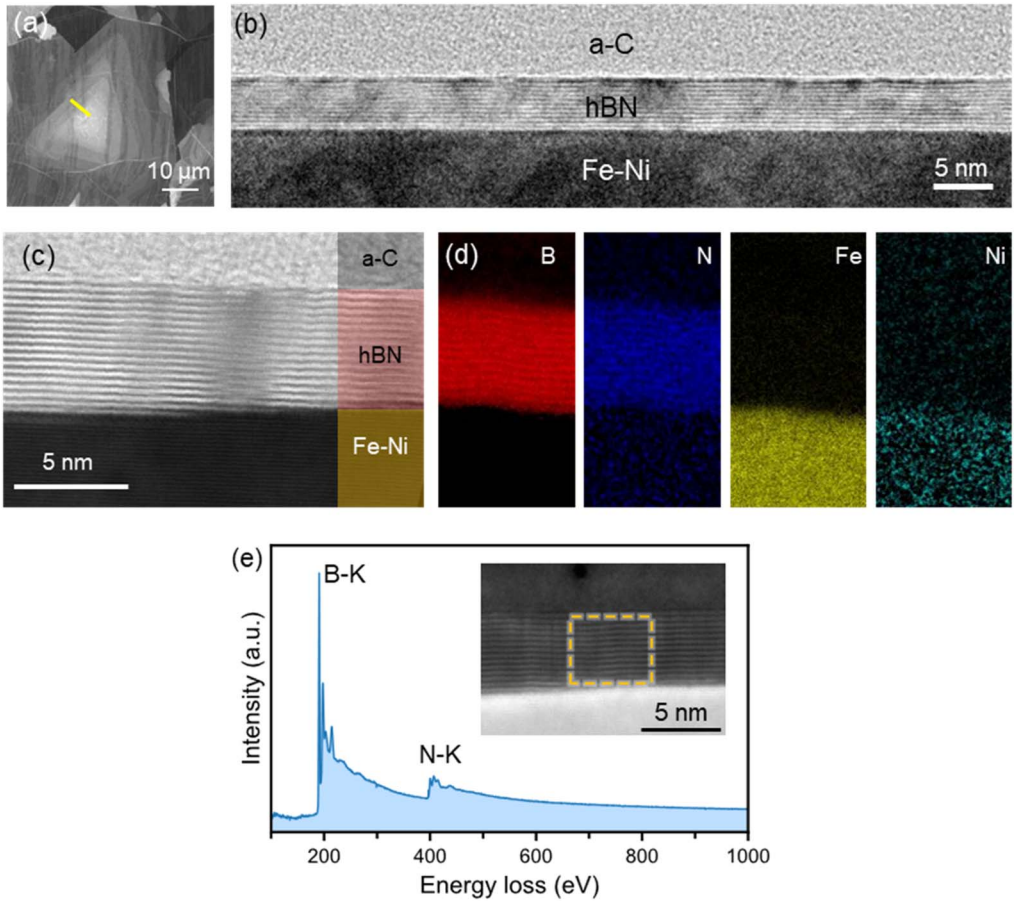

Fig. 3 (a) SEM image of a triangular pyramidal hBN grain used for the cross-section imaging. (b) Cross-sectional TEM image of the hBN grain grown on Fe–Ni foil. The TEM specimen was cut along the yellow line in (a). The hBN is protected from FIB process by pre-deposited amorphous carbon (a-C) layer. (c) Bright-field (BF) STEM image. (d) EELS elemental mapping of as-grown hBN. (e) EELS loss spectrum of the hBN collected from the area marked in the inset. Inset is the high-angle annular dark field (HAADF)-STEM image of the cross-section.

increasing from the bottom to the top. The Fe–Ni alloy has a positive CTE, expanding upon heating and contracting during cooling. In contrast, the in-plane CTE of hBN is negative, resulting in opposite behaviour. Owing to the difference between the CTEs of hBN and Fe–Ni, the as-grown hBN is supposed to experience compressive force from the Fe–Ni alloy during the CVD cooling process. The presence of compressive strain in the pyramid-shaped grains is further evidenced by the high density of wrinkles observed on the grain surface (Fig. 1c). In addition, it is worth noting that the strain remains in the multilayer hBN grains even after transfer to SiO_2 substrates, indicating that the strain is preserved in the multilayer films.

Here, we estimate the magnitude of the compressive strain applied to hBN using two approaches: (i) the difference in the CTE values of hBN and the Fe–Ni alloy and (ii) the shift of the observed sub-peak from the Raman E_{2g} band. The strain arising from the difference in the CTE values is estimated by considering the different volume changes of hBN and the underlying Fe–Ni foil. In this case, the strain induced in a two-dimensional material by the substrate can be expressed as follows:[41,43]

$$\varepsilon = \int_{T_0}^{T_{CVD}} \{\alpha_{2D}(T) - \alpha_{substrate}(T)\}\, dT \quad (1)$$

where T_{CVD} is the growth temperature, T_0 is the room temperature, and α_{2D} and $\alpha_{substrate}$ represent the TECs of the 2D material and growth substrate, respectively. Eqn (1) can be used to calculate the strain introduced during the cooling down step after the growth at high temperature. For the CTE value of hBN, we used the following equation[44] (Fig. S12a):

$$\alpha_{hBN}(T) = \left(-2.96 \times 10^{-6} + 3.83 \times 10^{-9} T\right) \quad [1/^\circ C] \quad (2)$$

The CTE of Fe–Ni alloy varies depending on its composition (*i.e.* Fe/Ni ratio). The Super Invar alloy used in this study is known to exhibit stepwise behaviour (Fig. S12b) following the empirical relationship:[45]

$$\alpha_{Super\ Invar}(T) = \begin{cases} -25.07 \times 10^{-9} + 2.32 \times 10^{-9} T\ (\sim 140^\circ C) \\ -10.36121 \times 10^{-6} + 76.25 \times 10^{-9} T\ (140 - 340^\circ C) \\ 12.96039 \times 10^{-6} + 7.23 \times 10^{-9} T\ \ (340^\circ C \sim)\ [1/^\circ C] \end{cases} \quad (3)$$

We plotted the strain calculated from eqn (1)–(3) in Fig. S12c. The maximum strain introduced in hBN is estimated to be −1.83% for $T_{CVD} = 1200$ °C and $T_0 = 27$ °C.

To experimentally estimate the in-plane strain stored in the hBN layers, we analysed the measured Raman shift between the sub-peak (interpreted as the blue-shifted E_{2g} mode of the strained bottom layers) and the E_{2g} band originating from the unstrained upper layers. Assuming isotropic thermal deformation of the metal in the in-plane direction, biaxial strain is supposed to be applied to the pyramid-shaped hBN grains. The relationship between the biaxial strain applied to hBN and the E_{2g} band shift is expressed by the following equation:[23]

$$\varepsilon = -\frac{\Delta\omega_{E_{2g}}}{2\gamma_{E_{2g}}\omega^0_{E_{2g}}} \quad (4)$$

where ε is the biaxial strain value, $\Delta\omega_{E_{2g}}$ is the shift of the E_{2g} band position, $\gamma_{E_{2g}}$ is the Grüneisen parameter of the E_{2g} band, and $\omega_{E_{2g}}{}^0$ (1367 cm^{-1}) is the frequency of the E_{2g} band without strain. The Grüneisen parameter was reported in a previous study using a three-point bending test to introduce uniaxial strain, where values of 1.04 for multilayer (>10 layers) samples and an average of 1.88 for 2–4 layers samples were obtained.[23] From eqn (4) the maximum compressive strain induced in the multilayer hBN grain is found to be -0.68 ± 0.02 ($\gamma_{E_{2g}} = 1.88$) to $-1.23 \pm 0.04\%$ ($\gamma_{E_{2g}} = 1.04$) corresponding to the maximum shift of 35 ± 1.25 cm^{-1} with respect to the E_{2g} band position. The calculation details are presented in Fig. S12d. We also calculated the strain for three other triangular pyramidal hBN grains, with the maximum strain at the centres ranging from −0.68 to −1.62% (Table S1). The calculated strain based on the Raman shift is slightly smaller than that estimated from the CTE differences between hBN and Fe–Ni (−1.83%). In addition to inaccuracies in the used Grüneisen parameter, this can be explained by the presence of wrinkles in the hBN sheet (see Fig. 1c), because the wrinkle formation can partly release compressive strain applied by the underlying metal catalyst. Additionally, the calculation method in eqn (1) assumes perfect transfer of the strain from the Fe–Ni substrate, but hBN may not fully follow the contraction of Fe–Ni due to slippage or other factors. Therefore, we can conclude that the sub-peak mainly originates from the strained hBN layers.

The shift of the sub-peak from the original E_{2g} band shown in Fig. 2b suggests that significant strain is concentrated near the centre of the pyramid-shaped grains. Fig. 4 illustrates the formation and compression processes of the pyramidal hBN grain during the CVD cooling. During the CVD process, hBN is formed *via* segregation of B and N atoms from nucleation sites on the metal foil. The observed strain concentration at the centre of these grains can be attributed to several complementary mechanisms. The compressive strain tends to concentrate at the centre of the grain due to its triangular geometry and the rigid structure consisting of many hBN layers. As shown in the cross-sectional STEM image (Fig. 3c), the increase in the thickness of hBN from the edge to the centre of the triangular grains arises from steps in the underlying Fe–Ni substrate. At the sites where pyramidal hBN grains grow, inverted pyramid-shaped pits are likely present on the Fe–Ni surface, with lateral dimensions decreasing with depth. We consider that hBN grows conformally within these pits, creating a pyramidal grain structure where lower layers have smaller lateral sizes and upper layers become progressively wider, as illustrated in Fig. 4. We consider that the strain in hBN upon cooling is mainly induced through these steps of the substrate (green arrows in Fig. 4). This can explain why the sub-peak is absent in flat regions of the hBN (outside the triangular flakes).

Another possible reason for the large strain at the grain centre is the large shrinkage of the metal foil at a nucleation site as compared with other surrounding areas, as the amount of B and N atoms dissolved in the metal foil can be very high (because most likely the B and N atoms remain at interstitial sites of the Fe–Ni lattice) so that B–N segregation induces a large volume change mostly at the nucleation sites (orange arrows in Fig. 4).

Finally, the strain distribution from thick to thin hBN layers might be further influenced by the temporal sequence of layer formation during cooling. The bottom layers near the grain centre nucleate and grow at higher temperatures than the top layers formed later, subjecting the earlier-formed layers to greater thermal contraction during the continued cooling process. This likely generates a vertical (*c*-axis) gradient of in-plane compressive strain. This interpretation is supported by the simultaneous presence of the E_{2g} band (~1367 cm^{-1}), attributed to unstrained hBN layers, and the sub-peak at higher wavenumbers, associated with blue-shifted E_{2g} phonons from the strained layers, across the whole pyramidal grain. This is also supported by Raman measurements performed on as-grown hBN on the Fe–Ni foil. In general, the Raman signal of hBN becomes significantly weaker when measured directly on the Fe–Ni substrate, likely due to strong interactions between hBN and the metal surface. For the pyramidal grains, the E_{2g} peak was barely detectable in the thin outer regions. While the E_{2g} peak was observed near the centre of the grain, the sub-peak was not detected (Fig. S13). This suggests that the lower hBN layers, which are expected to be under higher strain, exhibit suppressed Raman signals due to stronger interactions with the metal, and that the observed signal likely originates from the unstrained upper layers.

Assuming the hypothesis that each layer experiences a different degree of in-plane strain along the vertical direction, the sub-peak, which was analysed as a single peak, could represent a superposition of several slightly blue-shifted E_{2g} components from the strained lower layers. As the hBN thickness increases, more strained layers contribute to this signal, each with varying strain levels, leading to the observed broadening of the sub-peak (Fig. S3).

These mentioned mechanisms seem to collectively contribute to the observed strain increase at the centre of the pyramidal structures. However, it is worth noting that this sub-peak was observed only in triangular pyramidal grains with parallel stacking configurations and was not detected in grains with antiparallel stacking, which are presumed to have AA′ stacking (Fig. S14). This suggests that the stacking order may also influence the phonon behaviour in multilayer hBN

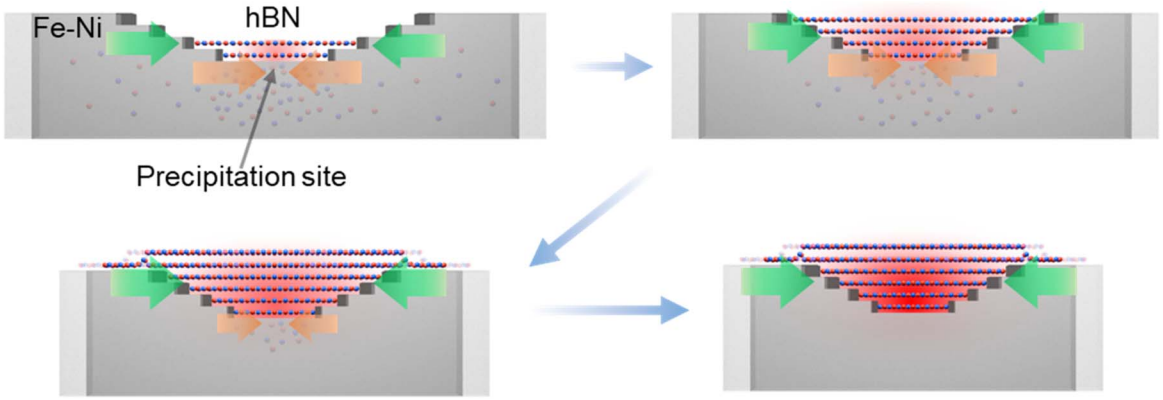

Fig. 4 Schematic showing the formation of a multilayer triangular pyramidal hBN grain *via* segregation of B and N atoms, and the compressive strain applied to the hBN grain from the underlying Fe–Ni alloy catalyst in the cooling step. The red shades in the hBN layers represent the compressive strain. Blue and red atoms indicate B and N atoms, respectively.

structures. In addition, previous studies have reported phonon polariton peaks on the high wavenumber side of the E_{2g} phonon in hBN, whose positions shift with the distance from the flake edge.[46,47] These features bear resemblance to the characteristics of the sub-peak observed in this work. However, phonon polaritons in hBN have so far been observed only near flake edges under near-field or electron-beam excitation, and it remains unclear whether they can be excited by visible light with a relatively large spot size as used in our Raman measurements. Therefore, while compressive strain remains the most plausible origin of the sub-peak, the possible influence of stacking configuration and phonon polariton effects will be further examined in future studies.

Finally, we note that the compressive strain determined from the Raman shift (−0.68 to −1.62%) in this study is much higher than the values reported in previous literature. The maximum compressive strain observed in the previous studies, except for high-pressure experiments, is −0.25% (see Table S2).[23,24,41,42,48–51] Therefore, the CVD growth can offer a new route toward strain engineering of hBN as well as other 2D materials.

Conclusions

We demonstrate that large compressive strain is introduced in single-crystalline hBN with a triangular pyramidal structure. This strain gives rise to an additional peak in the Raman spectrum, which shifts from 1380 cm^{-1} at the grain edges to 1415 cm^{-1} at the grain centre, while the position of the main E_{2g} band remains unchanged (1367 cm^{-1}). This large strain can be attributed to the difference in the CTE values of hBN and the growth substrate, in our case the Fe–Ni alloy catalyst. The maximum strain estimated from the Raman shift ranges from −0.68 to −1.62%, which is of the same magnitude as the strain determined from the difference in CTE values between hBN and the Fe–Ni foil. This strain is notably large compared to that reported in other experiments involving compressive strain. These findings are significant for understanding the stress state of hBN and suggest that controlling the strain (or strain engineering) can open new avenues for enhancing material properties and device applications.

Conflicts of interest

The authors declare no conflict of interest.

Data availability

Data and research materials will be available on request.

The data supporting this article have been included in the article and its SI. See DOI: **https://doi.org/10.1039/d5na00283d**.

Acknowledgements

This work was supported by JSPS Grant-in-Aid for Scientific Research on Innovative Areas “Science of 2.5 Dimensional Materials: Paradigm Shift of Materials Science Toward Future Social Innovation” (KAKENHI grant numbers JP21H05232, JP21H05233, JP21H05235, JP22H05478, and 24H01165), JSPS KAKENHI grant numbers JP24H00407, JP23K17863, JP22F22358, JP23H00097, JP23K17756, JP25K01748 and JP25K08435, JST CREST grant numbers JPMJCR20B1, JMJCR20B5 and JPMJCR23A2, JST SPRING grant number JPMJSP2136, the National Research Foundation of Korea grant numbers NRF-RS-2024-00336324 and NRF-RS-2024-00411134, and the ERC “MORE-TEM” (951215) project. Part of the present experiments was carried out by using a facility at the Research Center for Ultra-High Voltage Electron Microscopy, The University of Osaka.

References

1 K. Watanabe, T. Taniguchi and H. Kanda, *Nat. Mater.*, 2004, **3**, 404–409.
2 Z. Liu, Y. Gong, W. Zhou, L. Ma, J. Yu, J. C. Idrobo, J. Jung, A. H. MacDonald, R. Vajtai, J. Lou and P. M. Ajayan, *Nat. Commun.*, 2013, **4**, 2541.

3 L. H. Li, J. Cervenka, K. Watanabe, T. Taniguchi and Y. Chen, *ACS Nano*, 2014, **8**, 1457–1462.
4 A. Falin, Q. Cai, E. J. G. Santos, D. Scullion, D. Qian, R. Zhang, Z. Yang, S. Huang, K. Watanabe, T. Taniguchi, M. R. Barnett, Y. Chen, R. S. Ruoff and L. H. Li, *Nat. Commun.*, 2017, **8**, 15815.
5 C. R. Dean, A. F. Young, I. Meric, C. Lee, L. Wang, S. Sorgenfrei, K. Watanabe, T. Taniguchi, P. Kim, K. L. Shepard and J. Hone, *Nat. Nanotechnol.*, 2010, **5**, 722–726.
6 F. Withers, T. H. Bointon, D. C. Hudson, M. F. Craciun and S. Russo, *Sci. Rep.*, 2014, **4**, 4967.
7 S. Ahn, G. Kim, P. K. Nayak, S. I. Yoon, H. Lim, H.-J. Shin and H. S. Shin, *ACS Nano*, 2016, **10**, 8973–8979.
8 H. Ago, S. Okada, Y. Miyata, K. Matsuda, M. Koshino, K. Ueno and K. Nagashio, *Sci. Technol. Adv. Mater.*, 2022, **23**, 275–299.
9 S.-B. Song, S. Yoon, S. Y. Kim, S. Yang, S.-Y. Seo, S. Cha, H.-W. Jeong, K. Watanabe, T. Taniguchi, G.-H. Lee, J. S. Kim, M.-H. Jo and J. Kim, *Nat. Commun.*, 2021, **12**, 7134.
10 T. T. Tran, C. Elbadawi, D. Totonjian, C. J. Lobo, G. Grosso, H. Moon, D. R. Englund, M. J. Ford, I. Aharonovich and M. Toth, *ACS Nano*, 2016, **10**, 7331–7338.
11 K. Yasuda, E. Zalys-Geller, X. Wang, D. Bennett, S. S. Cheema, K. Watanabe, T. Taniguchi, E. Kaxiras, P. Jarillo-Herrero and R. Ashoori, *Science*, 2024, **385**, 53–56.
12 S. Emoto, H. Kusunose, Y.-C. Lin, H. Sun, S. Masuda, S. Fukamachi, K. Suenaga, T. Kimura and H. Ago, *ACS Appl. Mater. Interfaces*, 2024, **16**, 31457–31463.
13 Y. Uchida, T. Iwaizako, S. Mizuno, M. Tsuji and H. Ago, *Phys. Chem. Chem. Phys.*, 2017, **19**, 8230–8235.
14 J.-H. Park, J. C. Park, S. J. Yun, H. Kim, D. H. Luong, S. M. Kim, S. H. Choi, W. Yang, J. Kong, K. K. Kim and Y. H. Lee, *ACS Nano*, 2014, **8**, 8520–8528.
15 S. M. Kim, A. Hsu, M. H. Park, S. H. Chae, S. J. Yun, J. S. Lee, D.-H. Cho, W. Fang, C. Lee, T. Palacios, M. Dresselhaus, K. K. Kim, Y. H. Lee and J. Kong, *Nat. Commun.*, 2015, **6**, 8662.
16 S. Fukamachi, P. Solís-Fernández, K. Kawahara, D. Tanaka, T. Otake, Y.-C. Lin, K. Suenaga and H. Ago, *Nat. Electron.*, 2023, **6**, 126–136.
17 P. B. Mirkarimi, K. F. McCarty and D. L. Medlin, *Mater. Sci. Eng., R*, 1997, **21**, 47–100.
18 H. Henck, D. Pierucci, G. Fugallo, J. Avila, G. Cassabois, Y. J. Dappe, M. G. Silly, C. Chen, B. Gil, M. Gatti, F. Sottile, F. Sirotti, M. C. Asensio and A. Ouerghi, *Phys. Rev. B*, 2017, **95**, 085410.
19 D. Liu, X. Chen, Y. Yan, Z. Zhang, Z. Jin, K. Yi, C. Zhang, Y. Zheng, Y. Wang, J. Yang, X. Xu, J. Chen, Y. Lu, D. Wei, A. T. S. Wee and D. Wei, *Nat. Commun.*, 2019, **10**, 1188.
20 R. Singhal, E. Echeverria, D. N. McIlroy and R. N. Singh, *Thin Solid Films*, 2021, **733**, 138812.
21 R. V. Gorbachev, I. Riaz, R. R. Nair, R. Jalil, L. Britnell, B. D. Belle, E. W. Hill, K. S. Novoselov, K. Watanabe, T. Taniguchi, A. K. Geim and P. Blake, *Small*, 2011, **7**, 465–468.
22 M. Krečmarová, D. Andres-Penares, L. Fekete, P. Ashcheulov, A. Molina-Sánchez, R. Canet-Albiach, I. Gregora, V. Mortet, J. P. Martínez-Pastor and J. F. Sánchez-Royo, *Nanomaterials*, 2019, **9**, 1047.
23 Ch. Androulidakis, E. N. Koukaras, M. Poss, K. Papagelis, C. Galiotis and S. Tawfick, *Phys. Rev. B*, 2018, **97**, 241414.
24 E. Blundo, A. Surrente, D. Spirito, G. Pettinari, T. Yildirim, C. A. Chavarin, L. Baldassarre, M. Felici and A. Polimeni, *Nano Lett.*, 2022, **22**, 1525–1533.
25 M. Nakatani, S. Fukamachi, P. Solís-Fernández, S. Honda, K. Kawahara, Y. Tsuji, Y. Sumiya, M. Kuroki, K. Li, Q. Liu, Y.-C. Lin, A. Uchida, S. Oyama, H. G. Ji, K. Okada, K. Suenaga, Y. Kawano, K. Yoshizawa, A. Yasui and H. Ago, *Nat. Electron.*, 2024, **7**, 119–130.
26 D. Erb, *Pybaselines*, version 1.0.0, DOI: **10.5281/zenodo.7255880**, Zenodo, 2022.
27 M. Newville, R. Otten, A. Nelson, T. Stensitzki, A. Ingargiola, D. Allan, A. Fox, F. Carter and M. Rawlik, *LMFIT: Non-Linear Least-Squares Minimization and Curve-Fitting for Python (1.3.4)*, Zenodo, 2025, DOI: **10.5281/zenodo.16175987**.
28 C.-J. Kim, L. Brown, M. W. Graham, R. Hovden, R. W. Havener, P. L. McEuen, D. A. Muller and J. Park, *Nano Lett.*, 2013, **13**, 5660–5665.
29 Y. Li, Y. Rao, K. F. Mak, Y. You, S. Wang, C. R. Dean and T. F. Heinz, *Nano Lett.*, 2013, **13**, 3329–3333.
30 M. Lv, J. Wang, M. Tian, N. Wan, W. Tong, C. Duan and J. Xue, *Nat. Commun.*, 2024, **15**, 295.
31 L. Chen, K. Elibol, H. Cai, C. Jiang, W. Shi, C. Chen, H. S. Wang, X. Wang, X. Mu, C. Li, K. Watanabe, T. Taniguchi, Y. Guo, J. C. Meyer and H. Wang, *2D Mater.*, 2021, **8**, 024001.
32 C. K. Oliveira, E. F. A. Gomes, M. C. Prado, T. V. Alencar, R. Nascimento, L. M. Malard, R. J. C. Batista, A. B. De Oliveira, H. Chacham, A. M. De Paula and B. R. A. Neves, *Nano Res.*, 2015, **8**, 1680–1688.
33 S. Caneva, R. S. Weatherup, B. C. Bayer, R. Blume, A. Cabrero-Vilatela, P. Braeuninger-Weimer, M.-B. Martin, R. Wang, C. Baehtz, R. Schloegl, J. C. Meyer and S. Hofmann, *Nano Lett.*, 2016, **16**, 1250–1261.
34 V. Babenko, Y. Fan, V.-P. Veigang-Radulescu, B. Brennan, A. J. Pollard, O. Burton, J. A. Alexander-Webber, R. S. Weatherup, B. Canto, M. Otto, D. Neumaier and S. Hofmann, *2D Mater.*, 2020, **7**, 024005.
35 Y. Ji, B. Calderon, Y. Han, P. Cueva, N. R. Jungwirth, H. A. Alsalman, J. Hwang, G. D. Fuchs, D. A. Muller and M. G. Spencer, *ACS Nano*, 2017, **11**, 12057–12066.
36 H. Shi, M. Wang, H. Chen, A. Rousseau, J. Shu, M. Tian, R. Chen, J. Plo, P. Valvin, B. Gil, J. Qi, Q. Wang, K. Liu, M. Zhang, G. Cassabois, D. Wu and N. Wan, *ACS Appl. Mater. Interfaces*, 2025, **17**, 14660–14669.
37 R. Arenal, M. Kociak and N. J. Zaluzec, *Appl. Phys. Lett.*, 2007, **90**, 204105.
38 L. Khalil, C. Ernandes, J. Avila, A. Rousseau, P. Dudin, N. D. Zhigadlo, G. Cassabois, B. Gil, F. Oehler, J. Chaste and A. Ouerghi, *Nanoscale Adv.*, 2023, **5**, 3225–3232.

39 S. Lu, P. Shen, H. Zhang, G. Liu, B. Guo, Y. Cai, H. Chen, F. Xu, T. Zheng, F. Xu, X. Chen, D. Cai and J. Kang, *Nat. Commun.*, 2022, **13**, 3109.
40 F. Sun, Z. Hao, G. Liu, C. Wu, S. Lu, S. Huang, C. Liu, Q. Hong, X. Chen, D. Cai and J. Kang, *Nanoscale*, 2018, **10**, 4361–4369.
41 Q. Cai, D. Scullion, A. Falin, K. Watanabe, T. Taniguchi, Y. Chen, E. J. G. Santos and L. H. Li, *Nanoscale*, 2017, **9**, 3059–3067.
42 K. Bera, D. Chugh, A. Patra, H. H. Tan, C. Jagadish and A. Roy, *Solid State Commun.*, 2020, **310**, 113847.
43 G. H. Ahn, M. Amani, H. Rasool, D.-H. Lien, J. P. Mastandrea, J. W. Ager III, M. Dubey, D. C. Chrzan, A. M. Minor and A. Javey, *Nat. Commun.*, 2017, **8**, 608.
44 R. S. Pease, *Acta Cryst.*, 1952, **5**, 356–361.
45 Z. Rao, D. Ponge, F. Körmann, Y. Ikeda, O. Schneeweiss, M. Friák, J. Neugebauer, D. Raabe and Z. Li, *Intermetallics*, 2019, **111**, 106520.
46 Z. Shi, H. A. Bechtel, S. Berweger, Y. Sun, B. Zeng, C. Jin, H. Chang, M. C. Martin, M. B. Raschke and F. Wang, *ACS Photonics*, 2015, **2**, 790–796.
47 A. Konečná, J. Li, J. H. Edgar, F. J. García de Abajo and J. A. Hachtel, *Small*, 2021, **17**, 2103404.
48 X. Chen, X. Yue, L. Zhang, X. Xu, F. Liu, M. Feng, Z. Hu, Y. Yan, J. Scheuer and X. Fu, *Adv. Funct. Mater.*, 2024, **34**, 2306128.
49 M. A. Kriegel, K. M. Omambac, S. Franzka, F.-J. Meyer Zu Heringdorf and M. Horn-von Hoegen, *Appl. Surf. Sci.*, 2023, **624**, 157156.
50 B. Lyu, H. Li, L. Jiang, W. Shan, C. Hu, A. Deng, Z. Ying, L. Wang, Y. Zhang, H. A. Bechtel, M. C. Martin, T. Taniguchi, K. Watanabe, W. Luo, F. Wang and Z. Shi, *Nano Lett.*, 2019, **19**, 1982–1989.
51 A. Azizimanesh, A. Dey, S. A. Chowdhury, E. Wenner, W. Hou, T. Peña, H. Askari and S. M. Wu, *Appl. Phys. Lett.*, 2023, **123**, 043504.